Dielectric Charging Processes and Arcing Rates of High Voltage Solar Arrays

Mengu Cho* and Daniel E. Hastings†
Massachusetts Institute of Technology, Cambridge, Massachusetts 02139

When high-voltage solar arrays are used in the low Earth orbit environment, serious interactions are known to occur between the solar cell material and the surrounding plasma. Arcing is known to be one of the most severe interactions. The charging processes of the dielectric coverglass by charged particles are studied numerically. If there is a field emission site with a high electric field enhancement factor β on the interconnector, charging processes due to enhanced field electron emission (EFEE) can be initiated and lead to the collisional ionization in neutral gas desorbed from the coverglass. Based on this arcing onset model, an arcing rate is calculated for a high-voltage solar array and good agreement is found with experimental data.

Nomenclature

A = $1.54\times10^{-6}\times10^{4.52\sqrt{\phi_W}}/\phi_W$, A/V^2
A_{cell} = area of a solar cell, m^2
A_{chrg} = area of the coverglass that looses stored charge due to an arcing event, m^2
A_{int} = area of an interconnector, m^2
B = $6.53\times10^9\phi_w^{1.5}$, V/m
C_{diel} = capacitance per unit area, F/m^2
d = dielectric plate thickness, m
E = electric field, V/m
E_{dsp} = energy required to desorb one neutral particle, eV
E_e = electron emission energy, eV
E_i = electron incident energy on dielectric plate, eV
$h(\beta)$ = distribution function of field enhancement factor
I_{ram} = total ram current from ambient to computational domain, A/m
$j_{\text{cond}}(y)$ = ambient ion current density to conductor location y, A/m^2
j_e = incident electron current density to dielectric, A/m^2
$j_{ec}(y)$ = electron emission current density emitted from location y on the conductor, A/m^2
$j_{ee}(x)$ = secondary electron current density emitted from location x on dielectric, A/m^2
j_{en} = electron current density due to ionization of neutral gases, A/m^2
$j_{id}(x)$ = ion current density to location x on dielectric plate, A/m^2
j_{in} = ion current density due to ionization of neutral gases, A/m^2
j_{ram} = ram current density, en_oV_{orbit}, A/m^2
l = length of conductor gap between dielectric plates, m
N_{int} = total number of solar cell interconnectors on solar array
N_{es} = total number of emission sites on solar array
n_{es} = emission site density, m^{-2}
n_n = neutral density, m^{-3}
n_o = ambient ion density, m^{-3}
P = probability
R = arcing rate of entire solar array, s^{-1}
S = emission site area, m^2
s = distance from triple junction measured along dielectric surface, m
T_s = surface temperature of coverglass, K
V = bias voltage (<0), V
V_{orbit} = orbital velocity, 8 km/s at LEO
v_n = neutral velocity, m/s
β = field enhancement factor
γ_{ee} = secondary electron yield
γ_{ie} = ion-induced secondary electron yield
ΔQ = charge lost from coverglass front surface due to an arc, C
ϵ_d = dielectric constant of dielectric plate, F/m
η_{dsp} = desorption energy efficiency
λ = individual arcing rate, s^{-1}
σ = surface charge density, C/m^2
σ_{ion} = ionization cross section, m^2
τ_{EFEE} = EFEE charging time, s
τ_{ion} = ion charging time, s
ϕ = electric potential, V
ϕ_s = surface potential, V
ϕ_W = work function of conductor surface, eV
ω_p = plasma frequency, rad/s

I. Introduction

IN the future, increased activities in space will require large amounts of power, of the order of 100 kW to 1 MW. At this high power level, the loss of power in its transmission inside the spacecraft and the mass of the transmission line can be substantial. High-voltage power generation and transmission is one of the solutions that minimize the power loss and the mass of the transmission lines. At the present time, photovoltaic power generation is the most reliable means of power generation in space. It is planned that the power for the initial phase of the space station will be provided by a high-voltage solar array generating 160 V. When the voltage is increased to such a high value, however, we can no longer neglect the interaction between the solar array and the surrounding space plasma. This is especially true in the low Earth orbit (LEO) environment, where the plasma density is high ($10^5 \sim 10^6$ cm^{-3}). The known interactions between the solar array and the plasma are arcing on the negatively biased part of the solar array, current leakage to the plasma, enhanced drag due to Coulomb collisions, and sputtering of the solar cell material. Among them, arcing is known to be a severe problem. Arcing is typically defined as a sudden current pulse up to an order of an ampere during a time of the order of a microsecond or less. It causes electromagnetic interference

Received June 28, 1990; revision received Dec. 13, 1990; accepted for publication Dec. 28, 1990.

*Research Assistant, Department of Aeronautics and Astronautics.
†Class of 1956 Career Development Associate Professor of Aeronautics and Astronautics, Department of Aeronautics and Astronautics. Member AIAA.

(EMI) with instruments, enhanced sputtering of the solar cell material, and possible damage to the solar cell. In one space experiment, arcing was observed to occur at voltage as low as -200 V.[1]

Parks et al.[2] attributed the arcing current to enhanced field emission from the solar cell interconnector due to a dielectric layer and subsequent collisional ionization inside the layer. They proposed the field enhancement was due to unneutralized ions inside the dielectric layer on the conductor. A similar theory has been developed in the area of vacuum breakdown. Latham et al.[3,4] attribute the prebreakdown emission current from the cathode in vacuum to the enhanced field emission, due to microscopic insulating material on the metal surface. For high-voltage solar arrays, electron emission from the interconnector has been observed experimentally by Snyder et al.[5] In the work by Parks et al.,[2] however, the electric field outside the dielectric layer was assumed to be constant. In actuality, this electric field will change with time, due to the charging of the nearby dielectric coverglass. This important issue is one of those discussed in the present work.

Hastings et al.[6] proposed that the arc discharge occurs by ionization of neutral gas desorbed from the dielectric coverglass, due to electron stimulated desorption (ESD) by electrons emitted from the interconnector, and defined the breakdown condition by

$$\lambda_{mfp} \le d, \text{ therefore, } n_n \ge \frac{1}{\sigma_{\text{ion}} d} \tag{1}$$

The neutral density over the dielectric, n_n, is determined by the desorption probability per electron, the number of electrons colliding with the dielectric surface, the electron emission current from the conductor, and the thermal velocity of the desorbed neutrals. There are several experimental observations suggesting the involvement of neutral gas in the arcing onset. Kuninaka[7,8] observed luminosity on the dielectric surface near the interconnector and that the arcing rate decreased with the array temperature. Both of these observations can be explained by a neutral gas desorption model.

Whereas the enhanced electron emission model by Parks et al.[2] resembles the prebreakdown cathode electron emission in vacuum breakdown, the model by Hastings et al.[6] resembles the breakdown mechanism of vacuum surface flashover.[9] The vacuum surface flashover is defined as a discharge phenomena between two electrodes in vacuum bridged by insulator material. It has been proposed[9] that discharge occurs due to ionization of the neutrals that are desorbed from the insulator

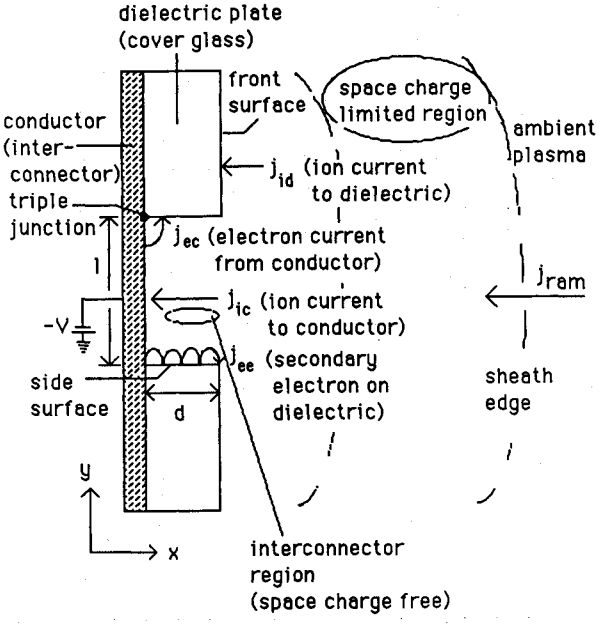

Fig. 1 Schematic view of system.

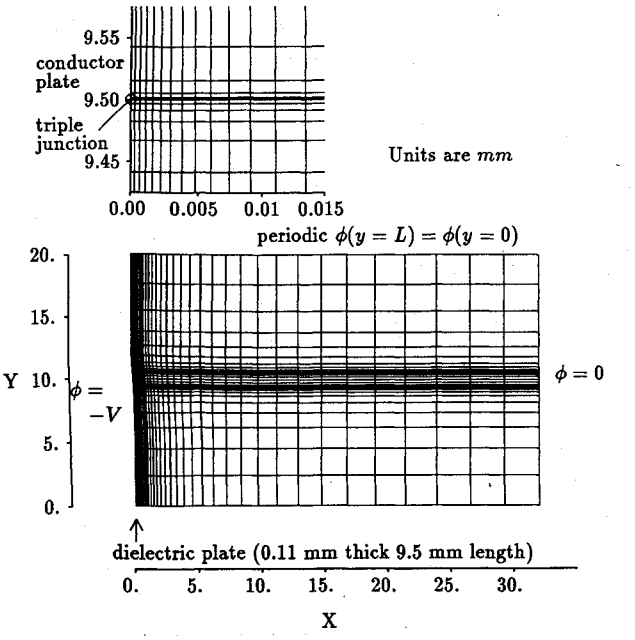

Fig. 2 Computational domain.

surface while the emitted electrons from the cathode travel toward the anode.

The application of vacuum surface flashover to solar array arcing seems promising, because the two phenomena have many aspects in common. But there are also differences between the two. The main differences are the following two points: 1) In solar array arcing, there is only one electrode, the interconnector, which acts as the cathode. The coverglass surface seems to act as the anode, but its potential is not fixed and is determined by charging due to charged particles from the ambient plasma. 2) In the solar array arcing, there are charged particles present that are neglected in the theory of vacuum surface flashover. The charged particles can charge not only the coverglass front surface but also the side surface corresponding to the insulator gap in the flashover. Both of these will significantly modify the electric field.

The purpose of this paper is to study the two effects and consider the breakdown mechanism by ionization of desorbed neutrals. We calculate the dielectric charging processes from the motion of the charged particles. The model system we consider is shown in Fig. 1. The important terminologies we use regarding the region of interest are *dielectric side surface,* the surface perpendicular to the conductor surface; *dielectric front surface,* the surface parallel to the conductor; *triple junction,* the point where the conductor, the dielectric, and the vacuum meet; and *interconnector region,* the region near the triple junction where the electric field is strong and the space charge is mostly neglected.

The rate of change of the surface charge density σ on the dielectric coverglass surface is given by

$$\frac{d\sigma(x,t)}{dt} = j_{id}(x,t) - \int P(x,y,t) j_{ec}(y,t)\, dy - \int P(x,x',t) j_{ee}(x')\, dx' + j_{ee}(x,t) - j_{en}(x,t) + j_{in}(x,t) \tag{2}$$

where $P(x,y,t)dx$ is the probability that the electron emitted from location y hits the dielectric surface in the range x to $x + dx$. In this paper we solve Eq. (2) numerically. For simplicity, we neglect the last two terms of Eq. (2), although they might be important during the arcing development. This means that we are only calculating arc initiation and not arc

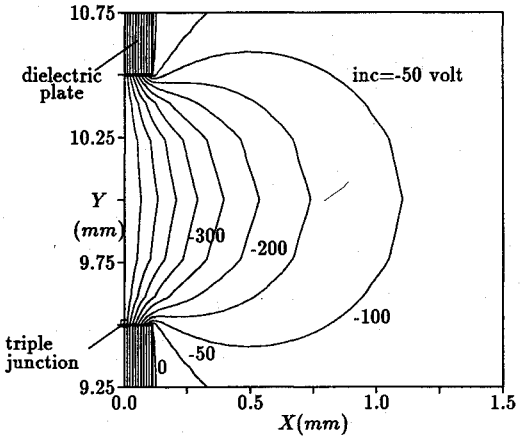

Fig. 3 Potential at the steady state for ion charging.

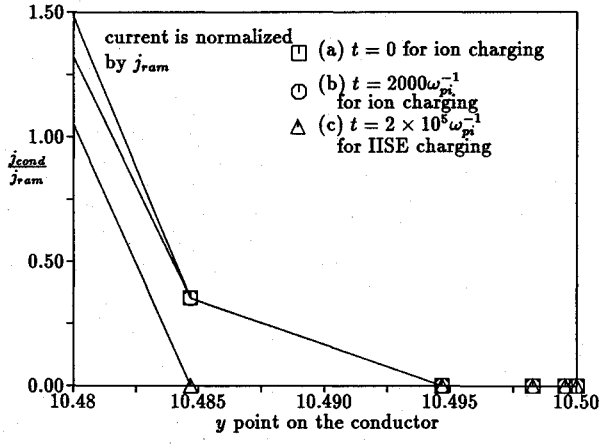

Fig. 4 Ion current distribution to the conductor.

development. We consider three charging mechanisms: charging due to ambient ions, charging due to ion-induced secondary electrons (IISE), and charging due to enhanced field emission electrons (EFEE).

In Sec. II, we discuss the numerical schemes used for each charging process. In Sec. III, we discuss the results of our numerical simulation. In Sec. IV, we develop a breakdown model using the results in Sec. III. In Sec. V, we calculate the arcing rate and compare to experimental data. In Sec. VI, we conclude the paper with a discussion of further work that is necessary.

II. Numerical Schemes

The model system we consider here consists of two 0.11-mm-thickness dielectric plates with $\epsilon_d = 2\epsilon_o$ (see Fig. 1), where 0.11 mm is a typical thickness of solar cell coverglasses and $\epsilon_d = 2\epsilon_o$ was chosen so that we could charge the dielectric plate quickly, while preserving the dielectric properties such as polarization. The plates sit on an underlying conductive plate with a 1-mm gap. The ambient plasma environment is $n_o = 5 \times 10^{11}\ \mathrm{m}^{-3}$ with $T_e = T_i = 0.1$ eV. The conductor plate is biased to -500 V, unless noted otherwise. The computational domain is shown in Fig. 2. Three types of numerical schemes were used.

A particle in cell (PIC) code was developed from PDW2[10] for a two-dimensional real space and a three-dimensional velocity space, with periodic boundaries in the y direction and Dirichlet boundary conditions in the x direction. We allow the grids to cluster around the interconnector. The dielectric plate is modeled by setting the charge density zero inside and accumulating all the arriving charges on the surface. A PIC code is used because it takes care of the space-charge effects automatically. These become significant in the EFEE charging. However, since PIC codes can be computationally expensive for long times, we have developed two orbit integration schemes that allow us to go to very long times for reasonable computational cost.

The scheme used for the charging of the system by collection of ions was a space-charge-limited orbit integration. The time scale for an ambient ion to travel from the sheath edge to the solar cell is of the order of the inverse ion plasma frequency. The change of the coverglass surface potential during time $1/\omega_{pi}$ is approximately $j_{\mathrm{ram}}/C_{\mathrm{diele}}/\omega_{pi} \approx 0.01$ V. Therefore, we can assume that the electric field is steady during the time an ambient ion travels from the sheath edge to the solar cell. Hence, the ion current to each point on the solar cell surface can be calculated by integrating the equation of motion for test particles from the sheath edge to the solar cell under a constant potential. The ion current density j_{id} is calculated by

$$j_{id}\,\mathrm{d}x = fI_{\mathrm{ram}} \tag{3}$$

where the factor f is the ratio of the number of test ions that reach locations from x to $x + \mathrm{d}x$ on the dielectric surface to the total number of test ions followed from the ambient (usually 3072). The surface charge density is then updated using only the first term in Eq. (2). We show later that the time scales of the first term and the rest of the terms in Eq. (2) are disparate. We then calculate the potential ϕ, solving the Poisson equation with the updated surface charge density. This process is repeated until it reaches a steady state. We neglect any incoming electron orbits and the magnetic field, since the bias on the conductor plate repels ambient electrons and the ion gyroradius for LEO is much larger than our system dimension.

The scheme used for the charging of the dielectric by electrons from the conductor is a space-charge-free orbit integration. We restrict the computational domain to $x = 4$ mm, and consider only $x = 0 \rightarrow 4$ mm, $y = 0 \rightarrow 20$ mm. This is reasonable for the electrons, since electrons escaping this domain will go outside the sheath without returning to the dielectric surface. In this domain, we can neglect space charge effects, as long as the electron current density is low. We neglect the first term in Eq. (2). We show later that the first term is already very small when the charging process, due to electrons, becomes significant. The secondary electron current at each point x is calculated by

$$j_{ee}(x,t) = \int \gamma_{ee}(x,y)P(x,y,t)j_{ec}(y,t)\,\mathrm{d}y + \int \gamma_{ee}(x,x')P(x,x',t)j_{ee}(x')\,\mathrm{d}x' \tag{4}$$

Then, the contribution to the rate of change of the surface charge density by electrons is given by

$$\frac{\mathrm{d}\sigma(x,t)}{\mathrm{d}t} = \int [\gamma_{ee}(x,y) - 1]P(x,y,t)j_{ec}(y,t)\,\mathrm{d}y + \int [\gamma_{ee}(x,x') - 1]P(x,x',t)j_{ee}(x')\,\mathrm{d}x' \tag{5}$$

where $\gamma_{ee}(x,x')$ is the secondary electron yield at the location x, due to the electrons emitted from the location x'. We integrate test electron orbits from the conductor, and calculate the secondary electron yield γ_{ee} and the impact probability P. Once we know $\gamma_{ee}(x,y)$, $\gamma_{ee}(x,x')$, $P(x,y)$, and $P(x,x')$ for a given $j_{ec}(y,t)$, we can solve Eqs. (4) and (5) for $\mathrm{d}\sigma/\mathrm{d}t$ and $j_{ee}(x,t)$. After we renew the surface charge density σ, we obtain the surface potential ϕ by the capacitance matrix method.[11] With the surface potential obtained, we solve the

Laplace equation to obtain the space potential, using the Schwarz-Christoffel transformation.[12]

We use the formula for γ_{ee}, given by Ref. 13:

$$\gamma_{ee} = \gamma_{\max}\frac{E_i}{E_{\max}}\exp\left(2-2\sqrt{\frac{E_i}{E_{\max}}}\right)\exp[2(1-\cos\theta_i)] \quad (6)$$

where $\gamma_{\max} = 2.9$ and $E_{\max} = 420$ eV are used as typical values for SiO_2. We consider two types of electron emission from the conductor. The first is an IISE emission by the ambient ion current. We set $j_{ec}(y) = \gamma_{ie} j_{\text{cond}}(y)$, where typically $\gamma_{ie} \simeq 0.1$.[14] The second mechanism is EFEE, which is given by

$$j_{ec}(y) = A(\beta E)^2 \exp\left(-\frac{B}{\beta E}\right) \quad (7)$$

This is the Fowler-Nordheim formula for field emission, with field enhancement factor β.[3] We assume that the electric field is enhanced by some mechanism such as dielectric impurities or microscopic structures on the conductor surface. Experimental data for field enhancement factors has been found to be $\beta \leq 100$ for metallic whiskers, and up to a few thousand for dielectric inclusions.[3,15] A reasonable value for ϕ_W is 4.5 eV for Cu, Mo, and Ag. For the field emitted electrons, we assumed cold emission, that is, the electrons are emitted with zero energy. For the secondary electrons, we assumed a Gaussian distribution for the energy and a cosine distribution for the emission angle.

III. Numerical Results

Ion Charging

We studied only the case of zero angle of attack, where the incoming ions have no drift velocity in the transverse direction at the boundary. An artificial ion mass, $m_i/m_e = 100$, was used. For the initial conditions, we chose $\phi_s = 0$ for the dielectric front surface and $\phi_s(x) = (V)(1-x/d)$ for the side surface. It is reasonable to assume that the front surface of the dielectric is charged much faster than the side surface because it has a smaller capacitance per unit area (typically by one or two orders of magnitude) than the side surface, estimating from the values of the capacitance matrix. In addition, for early times when the surface voltage is still highly negative, the ion orbits are not strongly deflected and strike the front surface on ballistic trajectories. The ion orbits must be highly deflected in order to strike the side surface for small angle of attack. We estimate that, at time $t \simeq (|V|\epsilon_d)/(dj_{id})$, the front surface is charged to $\phi_{\text{front}} \simeq 0$ and the side surface is still left uncharged. The numerical result indicates that, after $2000\omega_{pi}^{-1}$, the current to the dielectric front surface becomes nearly zero. The front surface attains a steady state by gaining a potential $\phi_{\text{front}} \simeq 5$ V just positive enough to repel the incoming 5-eV ion flow. The potential contours around the interconnector are shown in Fig. 3. The ions entering the interconnector region cannot hit

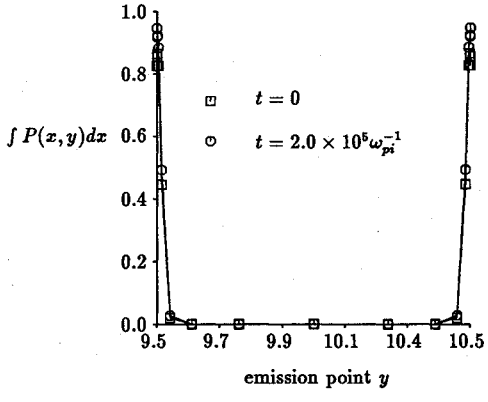

Fig. 5 Probability that electrons emitted from point y hit any part of dielectric surface.

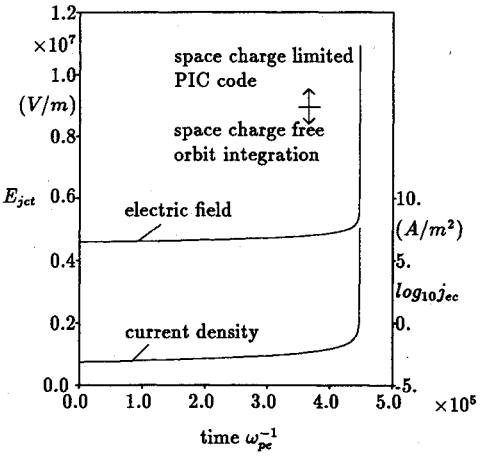

Fig. 6 Time history of electric field and current density at the triple junction due to the enhanced field electron emission charging.

the dielectric side surface for zero angle of attack. The current distribution on the conductor near the triple junction is shown as curves (a) and (b) in Fig. 4. The ions never strike the vicinity of the triple junction that corresponds to the 10.5-mm point in the figure. We followed 3×10^5 ions as a special case, and confirmed that no ions hit the dielectric side surface for zero angle of attack. This enables us to bound the ion current to the side surface as being less than $6 \times 10^{-4}\, j_{\text{ram}}$. This is significantly smaller than the electron current to the side surface considered in the next section.

Electron Charging

As the initial condition for both types of electron charging, the steady state obtained by the ion charging shown in Fig. 3 is used. This implies that we neglect the charging due to the electrons until that point. If the electron emission is due to the IISE, the ion current to the conductor is small while it is still charging the dielectric surface. If the electron emission is due to the EFEE, the electric field in the interconnector region is small until the coverglass front surface becomes grounded. Therefore, for both cases of emission mechanism, the electron emission current is negligible until ions cease to charge the dielectric surface. Therefore, the first term and the rest of terms in Eq. (2) are decoupled and calculated separately.

IISE Charging

For the ion current j_{cond}, we used the current density obtained at 2000 ω_{pi}^{-1} in the ion charging calculation. The electrons emitted from the conductor mainly strike the dielectric side surface near the corner. In most parts of the dielectric surface, the number of secondary electrons leaving the surface exceeds the number of incoming electrons. Due to this positive charging, the potential over the side surface and the electric field at the triple junction increases. The time scale of this charging process is one order of magnitude longer than that of ion charging calculated in the previous section, because the capacitance of the side surface is larger than the front surface and the current density is smaller than the previous one.

In order to see how the electron charging affects the ion current density to the conductor, we calculated the ion orbits determined by the potential at $t = 1.5 \times 10^5\, \omega_{pi}^{-1}$. The result is shown as curve (c) in Fig. 4. The ion current tends to concentrate away from the triple junction as time goes on. This is because, as the side surface potential goes up due to the electron charging, it causes the normal electric field to increase and deflects the ion trajectories away from the triple junction. We calculated the probability that the emitted electrons, from a point on the conductor, impact any part of the dielectric surface. The probability is shown in Fig. 5. The electrons that impact the surface are only those emitted from near the triple junction. From Figs. 4 and 5, we can see that no electron from

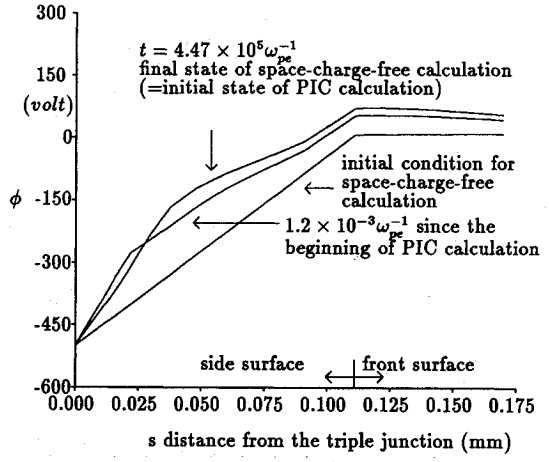

Fig. 7 Dielectric surface potential during EFEE charging.

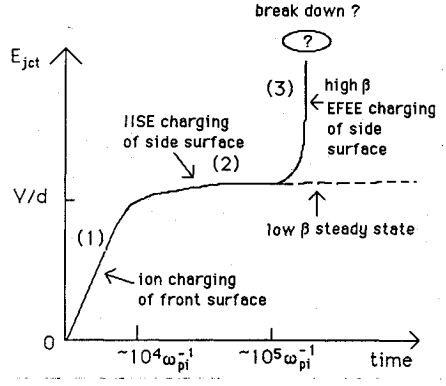

Fig. 8 Schematic picture of time history of electric field at the triple junction.

the conductor can hit the dielectric surface at $t = 1.5 \times 10^5 \omega_{pi}^{-1}$. We can, therefore, regard this as the steady state.

EFEE Charging

The steady state on the dielectric side surface reached by the IISE charging is steady as long as the charging due to enhanced field electron emission current is negligible. For small β (for our geometry approximately $\beta \leq 200$), we can neglect the effect of the EFEE charging. On the other hand, if β is large enough, once the emission current becomes substantial, the EFEE charging of the side surface develops very rapidly because of its exponential dependence on the field E, and we no longer have a viable steady state. In order to ascertain values that are significant, we calculate the value of β at which the emission current j_{ec} is comparable to the ambient ion ram current j_{ram}. For our geometry, the electric field is initially $E = 500/0.11$ mm $= 4.5 \times 10^6$(V/m) and the choice $j_{ec} \simeq j_{\text{ram}}$ gives $\beta = 345$.

For simplicity we assume $\beta = 345$ uniformly over the conductor surface. We use the same initial condition as the one used in the IISE charging. We show the time history of the electric field and the emission current density at the triple junction in Fig. 6. As the current goes up, we can no longer neglect the space charge effects produced by the emission current itself, and we have used the PIC code after $t = 4.47 \times 10^5 \omega_{pe}^{-1}$. As time goes on, the surface attains the steady state $j = 0$ from the corner $s = d$, and the positive current peak moves closer to the triple junction. We show the dielectric surface potential during the EFEE charging in Fig. 7. The potential near the corner $s \simeq d$ increases during the initial phase of the charging due to the fact that $\gamma_{ee} > 1$, but decreases during the space-charge-limited charging (PIC calculation) as the secondary electron yield approaches unity. On the other hand, the potential near the triple junction $s \simeq 0$ keeps increasing, because there is still positive current due to the secondary electron multiplication. Therefore, the electric field at the triple junction is not bounded.

We also numerically calculated the rate of energy deposition per unit area on the dielectric surface after the secondary electrons are emitted. The rate is given by $j_e(E_i - \gamma_{ee}E_e)/e$, with $E_e = 2$ eV, and this value became as high as 10^8(W/m^2).

IV. Arcing Onset Mechanism

On the basis of the numerical calculations, we can draw a picture of how the solar cell dielectric is charged after the conductor reaches the bias potential. The time history of the electric field at the triple junction is shown schematically in Fig. 8.

Phases (1) and (2) occur for every solar cell on the solar array. Some of the solar cells might have a whisker or dielectric impurity on the conductor surface. This will enhance the electric field. If the enhancement is high enough, then EFEE charging is initiated and phase (3) in Fig. 8 develops rapidly. The emission current from the conductor becomes so substantial that we can no longer neglect desorption of neutral gas from the dielectric surface.

We now examine the possibility of electron collisional ionization of the desorbed neutral gas. The necessary condition for ionization is that there is at least one ionization collision while electrons travel through the gas. This condition is given by Eq. (1). Following the ionization of the neutral gas, there are several possible scenarios that can lead to the arcing. If the ionization can create enough ion current returning to the point near the triple junction on the conductor to cause a feedback effect, then a self-sustaining discharge (Townsend breakdown) will occur. It is also possible that the negative charges created by the ionization can quickly discharge the positive charges on the coverglass surface and change the potential structure in the interconnector region completely before any feedback effect begins. In this paper, we examine only the possibility of the

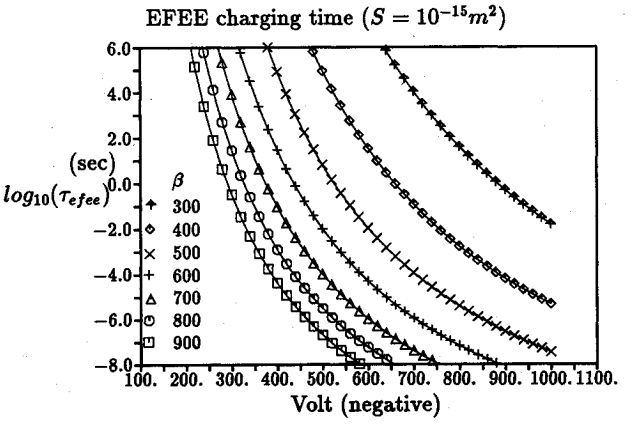

Fig. 9 Individual arc rate.

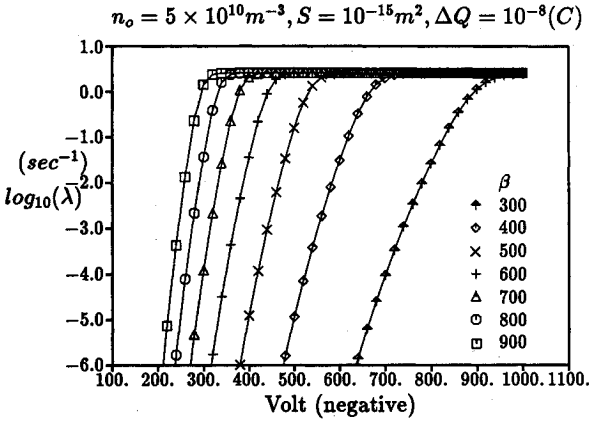

Fig. 10 EFEE charging time.

gas ionization. The necessary breakdown condition we take in the present paper is that the enhanced field electron emission will provide enough current to desorb a neutral cloud of the necessary density from the coverglass surface and it will begin to ionize.

For $\sigma_{ion} = 2 \times 10^{-20}$ m^2 and $d = 0.11$ mm, Eq. (1) gives the necessary neutral density $n_n \geq 4.5 \times 10^{23}$ m^{-3}. The electron energy flux 10^8 (W/m^2) to the dielectric flux, calculated numerically in the previous section, is too high to model the desorbed neutral flux by electron stimulated desorption.[16] Since the details of the desorption process are beyond the scope of this paper, we calculate the desorbed neutral flux simply by energy conservation. We define the desorption energy efficiency η_{dsp} as the fraction of incoming energy spent in desorption. Then the neutral density is given by

$$n_n = \frac{\eta_{dsp}}{E_{dsp}} \frac{\text{electron energy flux}}{v_n} = \frac{\eta_{dsp}}{E_{dsp}} \frac{j_e(E_i - \gamma_{ee}E_e)}{ev_n} \tag{8}$$

The neutral density satisfies the breakdown criteria $n_n \geq 4.5 \times 10^{23}$ m^{-3} at $\eta_{dsp} = 0.2$ for $E_{dsp} = 0.5$ eV and $v_n = 550$ (m/s), where a typical value for physisorption is used for E_{dsp} and $v_n = \sqrt{2\kappa T_s/m_n}$ for $T_s = 300$ K is assumed. We only have to spend 20% of the incoming energy in the desorption. In Eq. (8), the factor $\eta_{dsp}(E_i - \gamma_{ee}E_e)/E_{dsp}$ corresponds to the desorption yield in the ESD, defined by the number of neutral particles desorbed per incident electron. For our parameters, this is an order of unity and much higher than the typical value 0.01 for ESD. Since we allow the heating of the surface, this high yield is not unreasonable.

V. Arcing Rate

In this section, we calculate the arcing rate of the solar array, based on the above arcing model. We assume that the final stage of arcing onset, that is, the collisional ionization of neutral gas, takes a negligible time compared to the overall charging time of the solar cell dielectric materials. We also assume that the neutral adsorption layer on the coverglass surface quickly recovers before the next arc occurs. Therefore, the arcing rate is determined by the charging time of dielectric coverglasses. The charging of coverglass is mainly done by ambient ions and field emitted electrons. When the discharge occurs, some of the stored charges in the coverglass are lost. There is an experimental observation that the coverglass potential drops significantly, up to a few hundred volts from the steady-state value of $\phi_s \sim +5$ V during the discharge.[17] Before the next discharge occurs at the same point, we have to wait for the coverglass to recover the lost charges. We assume that the coverglass restores its lost charge through the ambient ions, because the electric field at the triple junction also drops after the discharge and the field emission ceases to charge the coverglass surface. After the coverglass charge is recovered so that the electric field becomes $E = V/d$ at the triple junction again, the same EFEE charging starts and results in the next discharge. This sequence is repeated with a period of $1/\tau_{total} = 1/(\tau_{ion} + \tau_{EFEE})$, and we define this as the arcing rate of this *arcing site*, $\lambda = 1/\tau_{total}$, assuming that every emission site survives the arcing. In experiments, arcing rates have been measured by counting the number of arcing occurrences for the entire test sample for a given time. In this paper, we calculate both the individual arc rate λ and the total arc rate R.

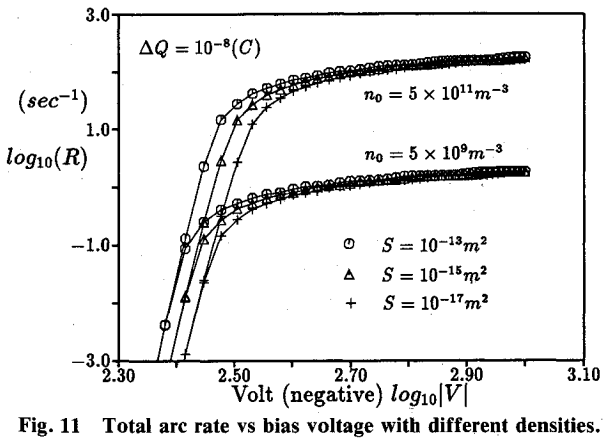

Fig. 11 Total arc rate vs bias voltage with different densities.

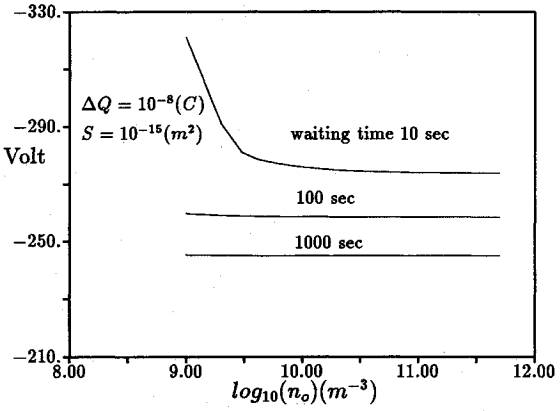

Fig. 12 Pseudo threshold voltage as a function of ion density.

We consider an array where two adjacent solar cells are simply bridged by one interconnector and assume that in each interconnector at most only one arcing site exists. Even though there might be more than one emission site in one interconnector, the number of emission sites that can contribute the charging of dielectric surface is assumed to be, at most, one. This emission site corresponds to the arcing site. The validity of this assumption is discussed later.

Charging Time

We now calculate the charging times for the EFEE charging, τ_{EFEE}, and the ambient ion charging, τ_{ion}. In the previous sections, the EFEE charging time was calculated assuming that the entire conductor surface is covered uniformly by emission sites. In reality, the emission sites are scattered randomly on the conductor surface with finite areas. In this section we take into account the effect of finite area of the emission sites. Pictures taken by electron microscopes show the emission sites consist of particles of the order of the micron.[18] The emission sites often contain foreign elements such as aluminum, carbon, sulphur, silver, and so on. Although the size of the emission site particles is one μm, the emission area is not necessarily the same as the particle area. The direct measurement of emission site area S is impossible and is usually calculated by dividing the measured total current by the current density calculated from the Fowler-Nordheim formula with β and work function ϕ_W. The calculated values range widely from $S = 10^{-13}$ m^2 to $S = 10^{-18}$ m^2 for β up to a few thousands.[15]

The rate of change of the surface charge density by electrons at the first impact point $x = d_i$ on the dielectric surface is given by neglecting the second term in Eq. (5):

$$\int_0^{d_i} \frac{d\sigma}{dt}\, dx = \int \left[\int_0^{d_i} P(x,y,t)\, dx \right] (\gamma_{ee} - 1) j_{ec}(y,t)\, dy \tag{9}$$

The integral $\int_0^{d_i} P(x,y,t)\, dx$ is approximately unity, since the point $x = d_i$ is the first impact point of the emitted electrons from the conductor surface. Then Eq. (9) simplifies as

$$\frac{d\sigma}{dt} d_i = (\gamma_{ee} - 1) j_{ec}(y,t) \sqrt{S} \tag{10}$$

The electric field on the conductor surface is approximately

$$E = \frac{\sigma}{C_{diel} d_i} \tag{11}$$

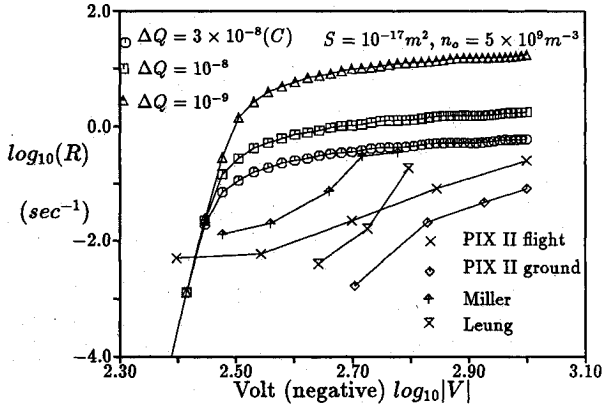

Fig. 13 Total arc rate vs bias voltage.

where the capacitance is for the side surface. Therefore, the rate of change of the electric field is given by

$$\frac{dE}{dt} = \frac{(\gamma_{ee} - 1)j_{ec}(y,t)[\sqrt{S}/d_i]}{C_{diel}d_i} \tag{12}$$

We integrate Eqs. (6) (with $E_i = Ed_i$ and $\theta_i = \pi/2$), (7), and (12) from $E = V/d$ until the current density j_{ec} shows a very sharp increase, as shown in Fig. 6. Since the current density j_{ec} has an exponential dependence on the electric field E, we can easily define this time within a small error. We take this time as the EFEE charging time τ_{EFEE}. The parameters used for the numerical integrations are $d = 0.15$ mm, $d_i = d/3 = 0.05$ mm, $C_{diel} = 9 \times 10^{-6}$ (F/m^2), $\phi_W = 4.5$ eV, $E_{max} = 420$ eV, and $\gamma_{max} = 2.9$. Those numbers are chosen to simulate a typical solar cell used in experiments.

The ambient ion charging time is calculated by

$$\tau_{ion} = \frac{\Delta Q}{j_{id}A_{chrg}} \tag{13}$$

The ion current density is given by

$$j_{id} = \epsilon n_o e V_{orbit} \tag{14}$$

where ϵ represents the ion focusing factor by the electric sheath, and is approximately $\epsilon = A_{cell}/A_{chrg}$. Then, the ion charging time is written as

$$\tau_{ion} = \frac{\Delta Q}{en_o V_{orbit}A_{cell}} \propto \frac{1}{n_o} \tag{15}$$

It should be noted that this assumption, in the present study, allows no voltage dependence to the ion charging time. In the case of ground based experiments, V_{orbit} is replaced by ion thermal speed. The charge lost from the coverglass surface is bounded by $\Delta Q \le \epsilon_d A_{cell} V_{bias}/d$. In this paper, we vary the value of ΔQ from 10^{-9} (C) to 10^{-7} (C), which corresponds to a voltage drop of the front surface $\Delta V = 10 \approx 1000$ V.

Arc Rate

We first calculate the arc rate of a single arc site. The individual arc rate λ is given by

$$\lambda = \frac{1}{\tau_{ion} + \tau_{EFEE}} \tag{16}$$

We show the result for $\Delta Q = 10^{-8}$ (C), $S = 10^{-15}$ m^2 and $n_o = 5 \times 10^{10}$ m^{-3} in Fig. 9. In the figure, the saturated arc rate $\lambda \approx 2.5$ (s^{-1}) indicates that the arc rate is determined by the ion charging time, i.e., $\tau_{ion} \gg \tau_{EFEE}$. On the other hand, $\lambda \ll 2.5$ indicates that $\tau_{ion} \ll \tau_{EFEE}$. For high-bias voltage and high β, the ion charging governs the total charging time. On the other hand, for low-bias voltage and low β the EFEE charging determines the total charging time. When the arcing rate is governed by ion charging, it does not depend on the bias voltage. This is because we neglected the voltage dependence in the ion charging time. However, even if it were included, it would be far less than the bias voltage dependence of the EFEE charging. This is shown in Fig. 10.

Another thing we should note here is that there is a *threshold* voltage for each β if we define it as the voltage which gives $\lambda = 0.0001$, that is, there is no arc within 10^4 s at less than this bias voltage. Since the ion charging time is much shorter than 10^4 s, the threshold voltages are determined only by the EFEE charging time. The time 10,000 s is approximately one orbital period in LEO. The threshold voltages are shown in Table 1.

We have assumed that the neutral adsorption layer on the dielectric surface recovers quickly, compared to the charging times. In most ground experiments, the ambient neutral densities were $n_n \simeq 3 \times 10^{17}$ m^{-3} [$p \sim 10^{-5}$ (Torr)]. With this density, it takes about 0.01 s to recover one neutral gas layer ($\simeq 10^{19}$ m^{-2}) lost due to the previous arc. Therefore, except for very dense plasmas and small ΔQ, our assumption is valid. In space, the recovery time seems to be much longer, due to the low ambient neutral density. However, since desorbed neutrals from the previous arc cause an increase in the neutral density over the coverglasses, the neglect of the time to rebuild the neutral gas layer is still reasonable.

We now calculate the total arc rate R. The total arc rate is given by

$$R = \int h(\beta)\lambda_\beta \, d\beta \tag{17}$$

where $h(\beta)\,d\beta$ is the number of interconnectors which have emission sites with value β to $\beta + d\beta$ near the triple junction. The term *near* means the place where the probability in Fig. 5 is nonzero. We assume that there is only one emission site near the triple junction in one interconnector. To confirm this, we consider a test sample consisting of 500 interconnectors with the area of 2×10^{-5} m^2 each. This is about the same as the PIX II flight sample (500 cells of 2 cm × 2 cm). We assume that the emission site density with $\beta > 250$ is $n_{es} = 1.4 \times 10^4$ m^{-2}, which is calculated from the results of Ref. 19. We should note here that experimental data regarding n_{es} is still very scarce, and this number can even be sample dependent. The total number of emission sites on an array is given by $N_{es} = n_{es}N_{int}A_{int}$. The probability that m emission sites are near the triple junction is $(1 - \Re)^{N_{es}-m}\Re^m N_{es}!/m!/(N_{es} - m)!$, where $\Re$ is the ratio of the area on the interconnector *near* the triple junction to the total area of the interconnector. The conditional probability that, given m sites are near the triple junction, all of those m sites are in different interconnectors is given by $N_{int}!/N_{int}^m/(N_{int} - m)!$. Then, taking the sum for all possible m, we obtain the probability that all the emission sites near the triple junctions are in different interconnectors as

$$\sum_{m=0}^{N_{es}} (1 - \Re)^{N_{es}-m}\Re^m \frac{N_{es}!}{m!(N_{es} - m)!} \frac{N_{int}!}{N_{int}^m(N_{int} - m)!} \tag{18}$$

We use $\Re = 0.05$ from the results shown in Fig. 5. This probability then becomes 95.29% for the present case. Therefore, we can safely assume that there is, at most, only one emission site near the triple junction in each interconnector. We consider a uniform distribution of β from $\beta = 250$ to 950. Then, $h(\beta)$ is given by $h(\beta) = N_{int} \times A_{int} \times n_{es} \times \Re \div (\beta_{max} - \beta_{min})$.

Figure 11 shows the arc rates for different ion densities. The arc rate R is linear with the ambient ion density at high voltage. The effects of the emission site area appear at low-bias voltage, and the curves with the same emission site area and the different ion densities merge at the low voltage. Therefore,

Table 1 Threshold voltage (negative)

β/S, m^2	10^{-13}	10^{-15}	10^{-17}
400	500	525	550
600	330	350	365
800	250	260	275
1200	165	175	185

the threshold voltage is independent of the ambient ion density and determined by the properties of the EFEE charging.

In experiments,[20] it has been suggested that the threshold voltage for arcing is density dependent. Ferguson[21] pointed out that this dependence could be explained solely on the basis of the waiting time at each voltage step. We confirm that hypothesis here by calculating the threshold voltage for an experiment of operation time τ. If we draw a horizontal line of $R = 1/\tau$ in Fig. 11, then intersections with our curves will correspond to the "threshold" voltage for each density. However, this "threshold" depends on how long we wait in the experiment. As we increase τ, the difference between the "threshold" voltages at different densities diminishes. Finally, if we wait long enough, there will be no difference in the "threshold" voltage for the different ion densities. Figure 12 shows this pseudo threshold voltage as a function of the ion density for the different waiting times. This pseudo threshold voltage for the different ion densities can be confirmed by an experiment that measures the change of threshold voltages with the operation time of the experiment.

Figure 13 shows the dependence of total arcing rate on the bias voltage. We also show the experimental results.[21,22,23] Since the experimental results cited in the figure have different parameters, we scaled the arcing rates of the experiments by $R \propto N_{\text{int}} A_{\text{int}}/\tau_{\text{ion}}$ to the arc rates that would have been if the experiments had had $n_o = 5 \times 10^9$ m^{-3}, $V_{\text{orbit}} = 8$ (km/s), $N_{\text{int}} = 500$, and $A_{\text{int}} = 2 \times 10^{-5}$ m^2. Ferguson[20] calculated the dependence of R on V by the least-square fit of the experimental results, and obtained $R \propto (-V)^{3\sim6}$. In our arcing model, there is no single power scaling between R and V. At the extreme high voltage, where $\tau_{\text{ion}} \gg \tau_{\text{EFEE}}$, the arc rate saturates. On the other hand, at the extreme low voltage, where $\tau_{\text{ion}} \ll \tau_{\text{EFEE}}$, there is a strong voltage dependence. At the moderate voltage, where τ_{ion} and τ_{EFEE} are comparable, the voltage dependence is determined by the combination of the ion charging time and the EFEE charging time. In the figure, as the ion charging time decreases (smaller ΔQ), the slope at the moderate voltage becomes higher. The shape of our curves at the moderate voltage agrees very well with the experimental results. The experimental results do not show the sudden drop at the low voltage, but this can be explained by the small amounts of data available at low voltages due to the finite waiting time in the experiments.

There is a large variance amounting to more than two orders of magnitude among the results shown in Fig. 13. This large variance of data can be explained by the insufficient sample numbers. The number of solar cells used in those experiments are very different. It was 24 of 2 cm × 2 cm cells for Leung's experiment and 4 of 4 cm × 2 cm cells for Miller's. For the emission site density $n_{es} = 1.4 \times 10^4$ m^{-2}, the expected total number of emission sites are only 6 for Leung's and 2 for Miller's, compared to 140 of PIX II.

One parameter that might have significant effect on the results is the coverglass thickness d. The parameter d enters the problem as the initial condition $E(t = 0) = V/d$ for the EFEE charging. This initial condition is based on the numerical result that ambient ions leave the side surface uncharged while they charge the front surface. However, as the thickness increases, we might anticipate an ion contribution to the charging of the side surface, and the initial condition for $E(t = 0)$ may be higher than V/d. The study of this effect of geometry will be done in future work.

VI. Conclusion

The results we have obtained are summarized as follows:

1) Ambient ions charge the dielectric front surface, leaving the side surface relatively uncharged.

2) Ion-induced secondary electrons from the conductor can charge the side surface and a steady state is obtained, unless enhanced field emission becomes significant.

3) Enhanced field electron emission (EFEE) can charge the side surface if the field enhancement factor is high. Once the EFEE charging is initiated it can lead to the collisional ionization of desorbed neutral from the coverglass surface.

4) For high-bias voltage and high field enhancement β, the ion charging time governs the total charging time and the arc rate. For low voltage and low β, the EFEE charging time dominates.

5) There is no single power scaling for the voltage dependence of total arc rate. It is determined by the combination of the ion charging time and the EFEE charging time.

6) There are well-defined bias voltage thresholds for each field enhancement factor β.

7) The threshold voltage is independent of the ambient ion density for very long experiment waiting times. It is possible to obtain the different threshold voltages for different ion densities, as possibly observed in the experiments with small waiting times.

8) We have obtained an arc rate that agrees reasonably well with experimental data and offers insight into interpreting that data.

In future work, the discharge processes of the desorbed neutral gas and the effect of geometry will be studied.

Acknowledgments

The authors would like to acknowledge useful suggestions from Guy Weyl of Physical Science, Inc. This research was supported by the Air Force Office of Scientific Research under Grant AFOSR-87-0340.

References

[1]Grier, N. T., "Plasma Interaction Experiment II (PIX II): Laboratory and Flight Results," *Spacecraft Environmental Interaction Technology—1983,* NASA CP-2359, March 1985, pp. 333-347.

[2]Parks, D. E., Jongeward, G. A., Katz, I., and Davis, V. A., "Threshold-Determining Mechanism for Discharges in High-Voltage Solar Arrays," *Journal of Spacecraft and Rockets,* Vol. 24, No. 4, 1987, pp. 367-371.

[3]Latham, R. V., *High Voltage Vacuum Insulation,* Academic Press, New York, 1981, pp. 178.

[4]Latham, R. V., "High Voltage Vacuum Insulation; New Horizons," *IEEE Transactions on Electrical Insulation,* Vol. 23, No. 5, 1988, pp. 881-894.

[5]Snyder, D. B., and Tyree, E., "The Effect of Plasma on Solar Cell Array Arc Characteristics," NASA-TM-86887, Jan. 1985.

[6]Hastings, D. E., Weyl, G., and Kaufman, D., "A Simple Model for the Threshold Voltage for Arcing on Negatively Biased High Voltage Solar Array," *Journal of Spacecraft and Rockets,* Vol. 27, No. 4, 1990, pp. 539-544.

[7]Kuninaka, H., Nozaki, Y., and Kuriki, K., "High Voltage Solar Array Interacting with Ionospheric Plasma," *Space Power,* Vol. 8, Nos. 1/2, 1989, pp. 51-68.

[8]Kuninaka, H., "Qualitative Experiments on Arc Discharges on Negatively Biased Solar Cells," *Journal of Spacecraft and Rockets,* Vol. 27, No. 6, 1990, pp. 665-668.

[9]Anderson, R. A., and Brainard, J. P., "Mechanism of Pulsed Surface Flashover Involving Electron-Stimulated Desorption," *Journal of Applied Physics,* Vol. 51, No. 3, 1980, pp. 1414-1421.

[10]Hastings, D. E., and Cho, M., "Ion Drag Coefficient for a Highly Negatively Biased Solar Array in LEO," *Journal of Spacecraft and Rockets,* Vol. 27, No. 3, 1990, pp. 279-284.

[11]Hockney, R. W., and Eastwood, J. W., *Computer Simulation Using Particles,* McGraw-Hill, New York, 1981, pp. 215-219.

[12]Hildebrand, F. B., *Advanced Calculus for Applications,* Prentice-Hall, Englewood Cliffs, NJ, 1976, pp. 641-652.

[13]Hachenberg, O., and Brauer, W., "Secondary Electron Emission from Solids," *Advancement in Electronics and Electron Physics,* Vol.

11, 1959, pp. 413-499.

[14]Thomas, E. W., "Secondary Electron Emission," *Data Compendium for Plasma-Surface Interactions,* in *Nuclear Fusion,* International Atomic Energy Association, Vienna, Austria, 1984, pp. 94-104.

[15]Noer, R. J., "Electron Field Emission from Broad-Area Electrons," *Applied Physics A,* Vol. A28, No. 1, 1982, pp. 1-24.

[16]Drinkwine, M. J., and Lichtman, D., "Electron Stimulated Desorption: A Critical Review," *Progress in Surface Science,* Vol. 8, No. 3, 1977, pp. 123-142.

[17]Snyder, D. B., "Discharge on a Negatively Biased Solar Cell Array in a Charged-Particle Environment," *Spacecraft Environmental Interaction Technology—1983,* NASA CP-2359, March 1985, pp. 379-388.

[18]Renner, Ch., Niederman, Ph., and Fisher, Ø., "Enhanced Field Emission Investigation of Aluminum," *IEEE Transactions on Electrical Insulation,* Vol. 24, No. 6, 1989, pp. 911-916.

[19]Latham, R. V., Bayliss, K. H., and Cox, B. M., "Spatially Correlated Breakdown Events Initiated by Field Electron Emission in Vacuum and High Pressure SF_6," *Journal of Physics D: Applied Physics,* Vol. 19, No. 12, 1986, pp. 219-231.

[20]Stevens, N. J., "Summary of Pix-2 Flight Results over the First Orbit," AIAA Paper 86-0360, Jan. 1986.

[21]Ferguson, D. C., "The Voltage Threshold for Arcing for Solar Cells in LEO-Flight and Ground Test Results," NASA-TM-87259, March 1986.

[22]Miller, W. L., "An Investigation of Arc Discharging on Negatively Biased Dielectric-Conductor Samples in Plasma," *Spacecraft Environmental Interaction Technology—1983,* NASA CP-2359, March 1985, pp. 367-377.

[23]Leung, P., "Characterization of EMI Generated by the Discharge of a 'Volt' Solar Array," NASA-CR-176537, Nov. 1985.

Alfred A. Vampola
Associate Editor